Int J Adv Manuf Technol (2017) 89:727–734
DOI 10.1007/s00170-016-9119-x

ORIGINAL ARTICLE

Numerical simulation of hump suppression in high-speed triple-wire GMAW

Yu Gu [1,2,3] · **Xueming Hua** [1,2,3] · **Dingjian Ye** [1,2,3] · **Fang Li** [1,2,3] · **Xiaoli Ma** [1,2,3] · **Chen Xu** [1,2,3]

Received: 10 March 2016 / Accepted: 26 June 2016 / Published online: 9 July 2016

Abstract A numerical model of a three-dimensional transient weld pool was conducted to analyze the hump formation mechanism in high-speed single-wire gas metal arc welding (GMAW) and the hump suppression in triple-wire GMAW. The effect of heat convection, radiation, and vaporization on temperature field and the impact of arc pressure, surface tension, Lorentz force, buoyancy force, and droplet impinging force on the fluid flow field were considered during simulations. In good agreement with the experimental beads and images recorded by high-speed camera, the simulated results are shown: during the hump formation in single-wire GMAW, the liquid channel was formed, elongated, pinched, and solidified due to the strong backward molten metal flow and the normal surface tension. However, in the same line energy, humps were suppressed in triple-wire GMAW. The "pull-push" flow in the triple-wire GMAW weld pool could dramatically slow down the backward trend, which reduced the solidification rate. Consequently, the liquid channel disappears and the humps could not be formed any more.

Keywords Triple-wire GMAW · Hump suppression · Numerical simulation · High-speed welding

✉ Xueming Hua
xmhua@sjtu.edu.cn

[1] School of Materials Science and Engineering, Shanghai, China

[2] Shanghai Key Laboratory of Materials Laser processing and Modification, Shanghai Jiao Tong University, Shanghai 200240, People's Republic of China

[3] Collaborative Innovation Center for Advanced Ship and Deep-Sea Exploration, Shanghai 200240, China

1 Introduction

The rapid development of modern manufacturing calls for higher welding efficiency, which can be improved by increasing welding speed. However, weld bead defects like hump, undercut, and other defects occur when the welding speed reaches a certain limit in single-wire gas metal arc welding (GMAW) [1–4]. As the hump defect severely restricts the improvement of welding efficiency, a lot of researchers have sought to better understand the process and mechanism of hump formation [5–7]. Bradstreet et al. [5] proposed a capillary instability model with the effect of surface tension, and the instability of liquid metal was the main factor in hump formation. This model was simplified as a free liquid cylinder, and other forces such as Lorentz force and arc pressure were ignored without any explanation when surface tension was identified as the main factor. Nguyen et al. [6, 7] found that the high-speed backward flow in the weld pool, which brought large amount of molten metal to the pool tail, was mainly responsible for the hump formation. He then designed uphill and downhill welding experiments to verify it with qualitative explanation. Cho et al. [8] studied the mechanism of hump formation through both simulations and experiments. He identified the pinching and early solidification of the narrow molten metal bead as the main factor of hump formation. Chen et al. [9, 10] established a numerical model for hump formation. The simulation results, which were in good agreement with experiments though Lorentz force was not considered, characterized the important role of backward flow of molten metal as well.

Other researches focused on the suppression of hump have proved that triple-wire GMAW can prevent hump formation and sequentially improve welding speed. In high-speed multi-wire GMAW, arc pressures are dispersed in the long weld pool, improving the stability of the pool,

thus reducing the tendency of undercut and hump defects. Hiroshi et al. [11] developed a triple-wire pulse welding controlled by current phase, which could reach 2.0 m/min in joint welding. During welding, the arcs were burning in turns of three wires and the energy distribution changed through adjusting the position of the three wires and inclination angle. Hang et al. [12] studied the effects of welding speed and welding current on the bead parameters in triple-electrode high-speed CO_2-shielded fillet welding, in which the max speed could reach 1.8 m/min. The length range of fillet leg is predicted when welding speed and triple electrode current combination change.

Although there are several researches on the hump formation, its mechanism has not reached a consensus. Few scholars pay attention to the hump suppression mechanism of triple-wire welding, and no one has ever analyzed it by simulation. In this study, using the finite element software FLOW-3D, a numerical model of a three-dimensional transient weld pool is established to study the hump formation mechanism in high-speed single-wire GMAW and the hump suppression mechanism in triple-wire GMAW.

2 Experimental procedure

As a guide and contrast of the simulations, experiments are conducted in the following conditions. Eight-millimeter-thick ASTM A36 steel is used as the workpiece of bead-on-plate welding, which material properties are listed in Table 1. The power supply is Panasonic YD-500GR3 welding power source and the welding wire is JM53 with the diameter of 1.2 mm. Ninety percent Argon + 10 % CO_2 is employed as the shielding gas, flowed at 20 L/min. The welding torch is kept perpendicular to the workpiece with a distance of 15 mm.

In the high-speed single-wire GMAW experiment, the welding current is 350 A, the welding voltage is 32 V, and the welding speed is 1.5 m/min. The images of the weld pool during hump formation are captured by a high-speed CCD camera (Fastcam-Super10KC, Photon) system with an optical band pass filter (808 ± 10 nm) and two polarizers. The frequency is set 300 frames/s.

In the triple-wire GMAW experiment, three wires are equally distributed in the distance of 20 mm along the welding direction. All the welding parameters are ensured in the same line energy with the single-wire GMAW. The leading/middle/trailing currents are set 300 A/240 A/240 A, the welding voltages are set 29 V/24 V/24 V, and the welding speed is set 2.7 m/min.

Table 1 Thermo-physical material properties of A36 steel

Nomenclature	Value
Density(s)	7800 (kg/m^3)
Density (l)	6900 (kg/m^3)
Viscosity	5.9×10^{-3} (kg/m s)
Thermal conductivity(s)	32.3 (W/m K)
Thermal conductivity (l)	26.9 (W/m K)
Specific heat(s)	686 (J/kg K)
Specific heat (l)	866 (J/kg K)
Latent heat of fusion	2.77×10^5 (J/kg)
Latent heat of vaporization	7.34×10^6 (J/kg)
Liquidus temperature	1798 (K)
Solidus temperature	1768 (K)
Vaporized temperature	2900 (K)
Heat transfer coefficient	100 (W/m^2 K)
Emissivity	0.5
Magnetic permeability	1.26×10^{-6} (H/m)
Coefficient of thermal expansion	10^{-4} (K^{-1})
Surface tension	1.2 (N/m)
Surface tension gradient	−0.0003 (N/m K)

3 Mathematical model and numerical simulation

The schematic models of single-wire GMAW and triple-wire GMAW are shown in Fig. 1.

To simplify the mathematical model, the following assumptions are made in this paper:

1. The molten metal is a Newtonian fluid and the flow is laminar and incompressible.

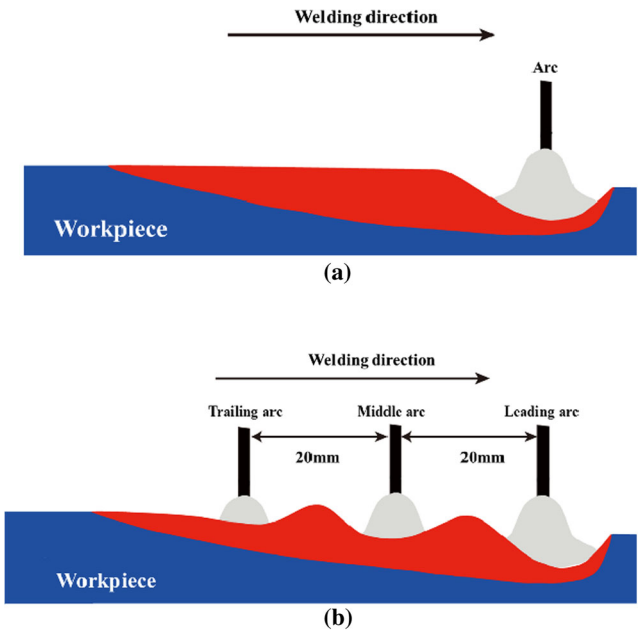

Fig. 1 **a** Single-wire GMAW. **b** Triple-wire GMAW

2. The material properties of A36 steel are assumed to be constant, except the surface tension which is temperature dependent.
3. The arcs are assumed to be stable during welding process, which means the interference between arcs is neglected in triple-wire GMAW.

3.1 Governing equations

In this paper, the dynamic behaviors of the weld pool are simulated by solving governing equations such as mass continuity equation, momentum equation, energy equation, and volume of fluid (VOF) method equation, which can track free surface of fluid.

Mass continuity equation:

$$\nabla\cdot\vec{V}=\frac{R_{SOR}}{\rho} \tag{1}$$

Momentum equation:

$$\frac{\partial\vec{V}}{\partial t}+\vec{V}\cdot\nabla\vec{V}=-\frac{1}{\rho}\nabla P+\nu\nabla^2\vec{V}+\vec{F}_b+\frac{R_{SOR}}{\rho}\vec{V}-K\vec{V} \tag{2}$$

Energy equation:

$$\rho\left[\frac{\partial U}{\partial t}+\vec{V}\cdot\nabla U\right]=-P\cdot\nabla\vec{V}+\nabla\cdot(k\nabla T)+U_{SOR}. \tag{3}$$

Considering the solid-liquid changes, the enthalpy-temperature relationship can be described as following formations:

$$h=C\rho T+f(T)L. \tag{4}$$

$$f(T)=\begin{cases}0 & (T\le T_s)\\ \dfrac{T-T_s}{T_l-T_s} & (T_s<T<T_l)\\ 1 & (T_l<T)\end{cases}. \tag{5}$$

VOF method equation:

$$\frac{dF}{dt}=\frac{\partial F}{\partial t}+\nabla\cdot\left(\vec{V}F\right) \tag{6}$$

where $\vec{V}$ is the molten metal velocity, ρ is liquid density, R_{SOR} is a mass source term, ν is kinematic viscosity, t is time, P is hydrodynamic pressure, $\vec{F}_b$ is body force, K is the drag coefficient for a porous media model, U is internal energy per unit mass, T is a local temperature, k is thermal conductivity, U_{SOR} is an energy source term, h is enthalpy, C is specific heat, L is the latent heat of fusion for phase change between liquid and solid, T_s and T_l are solidus and liquidus temperatures of the base metal, and F is a volume fraction of a fluid.

The body force $\vec{F}_b$ consists of Lorentz force and buoyancy force:

$$\vec{F}_b=\sum\vec{J}\times\vec{B}-\rho\beta g(T-T_0). \tag{7}$$

The Lorentz force of each arc can be obtained from the analytical solution [13], where $\vec{J}$ is the current density vector of each wire, $\vec{B}$ is the magnetic induction vector of each wire, β is the thermal expansion coefficient, and T_0 is ambient temperature.

3.2 Boundary conditions

The boundary conditions of top surface and other surfaces are different. On the top-free surface of the workpiece, the shear stress balance is described as follows:

$$\mu\frac{\partial u}{\partial z}=-\frac{\partial\gamma}{\partial T}\frac{\partial T}{\partial x} \tag{8}$$

$$\mu\frac{\partial v}{\partial z}=-\frac{\partial\gamma}{\partial T}\frac{\partial T}{\partial y} \tag{9}$$

where u and v are the velocity components in the x- and y-directions, μ is the dynamic viscosity, and γ is the surface tension.

The pressure boundary condition on the top surface is expressed as follows:

$$-p+2\mu\frac{\partial\vec{v}_n}{\partial n}=-\sum p_{arc}+\gamma\left(\frac{1}{R_1}+\frac{1}{R_2}\right) \tag{10}$$

where p is the liquid pressure in normal direction, $\vec{v}_n$ is the normal velocity vector, and R_1 and R_2 are the principal radii of surface curvature. The arc pressure p_{arc}, which is generated by each wire, can be expressed as below:

$$p_{arc}=\frac{\mu_0 I^2}{4\pi^2\sigma_x\sigma_y}\exp\left(-\frac{x^2}{2{\sigma_x}^2}-\frac{y^2}{2{\sigma_y}^2}\right) \tag{11}$$

where I is the welding current, μ_0 is the magnetic permeability, and σ_x and σ_x are the double elliptical distribution parameter.

On the top-free surface, convection, radiation, and evaporation are considered in the energy condition:

$$k\frac{\partial T}{\partial n}=\sum q(x,y,z)-q_{conv}-q_{rad}-q_{evap} \tag{12}$$

$$q_{conv}=h_c(T-T_0) \tag{13}$$

$$q_{rad}=\sigma\varepsilon\left(T^4-{T_0}^4\right) \tag{14}$$

$$q_{evap}=m_e M_b \tag{15}$$

where $q(x,y,z)$ is the heat source of each wire, q_{conv} is the heat loss of convection, q_{rad} is the heat loss of radiation, q_{evap} is the heat loss of evaporation, h_c is the heat transfer coefficient, σ is Stefan-Boltzmann constant, ε is the emissivity, m_e is the evaporation rate, and M_b is the latent heat of vaporization.

In paper, double ellipsoidal power density distribution is applied to describe the heat source of each arc [14]:

$$\begin{cases} q_f(x,y,z) = \dfrac{6\sqrt{3}f_f\eta UI}{a_f bc\pi\sqrt{\pi}}\exp\left(-\dfrac{3x^2}{{a_f}^2}-\dfrac{3y^2}{b^2}-\dfrac{3z^2}{c^2}\right), x\geq 0 \\ q_r(x,y,z) = \dfrac{6\sqrt{3}f_f\eta UI}{a_r bc\pi\sqrt{\pi}}\exp\left(-\dfrac{3x^2}{{a_r}^2}-\dfrac{3y^2}{b^2}-\dfrac{3z^2}{c^2}\right), x < 0 \end{cases} \quad (16)$$

where η is the efficiency of heat flux, U is the welding voltage, and I is the welding current. The fractions f_f and f_r present the heat deposition in the front and rear quadrants, where $f_f+f_r=2$. The shape of the heat source is decided by four independent parameters a_r, a_f, b, and c, which are shown in Fig. 2.

For other surfaces:

$$k\frac{\partial T}{\partial n} = -q_{conv}-q_{rad} \quad (17)$$

$$u = v = w = 0 \quad (18)$$

where u, v, and w are the velocity components in the x-, y-, and z-directions.

3.3 Surface tension

The surface tension of liquid metal is a complicated function of temperature, which is adopted in Sahoo's paper [15]. The formation is listed as follows:

$$\gamma = \gamma_m - A_r(T-T_m) - RT\Gamma_s\ln\left(1+k_l a_s\exp\left(-\Delta H_0/RT\right)\right). \quad (19)$$

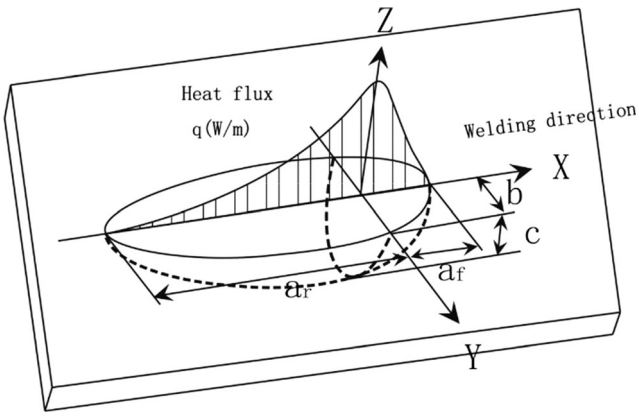

Fig. 2 Double ellipsoidal power density distribution of each arc's heat source

Therefore, the surface tension gradient can be described as follows:

$$\frac{d\gamma}{dT} = -A_r - R\Gamma_s\ln\left(1+k_l a_s\exp\left(-\Delta H_0/RT\right)\right) - \frac{k_l a_s\exp\left(-\Delta H_0/RT\right)}{\left(1+k_l a_s\exp\left(-\Delta H_0/RT\right)\right)T} \quad (20)$$

where γ_m is the surface tension of pure metal at the melting point, A_r is the surface tension gradient of pure metal at melting point, R is gas constant, Γ_s is the surface excess at saturation, k_l is the enthalpy factor, a_s is weight percent of sulfur, and ΔH_0 is the heat of absorption.

4 Results and discussion

4.1 Studies of hump formation in single-wire GMAW

The weld simulation results of bead-on-plate shape in high-speed single-wire GMAW are shown in Fig. 3a and the experimental ones are shown in Fig. 3b, both of which are in the same welding conditions. The simulated bead shows the same

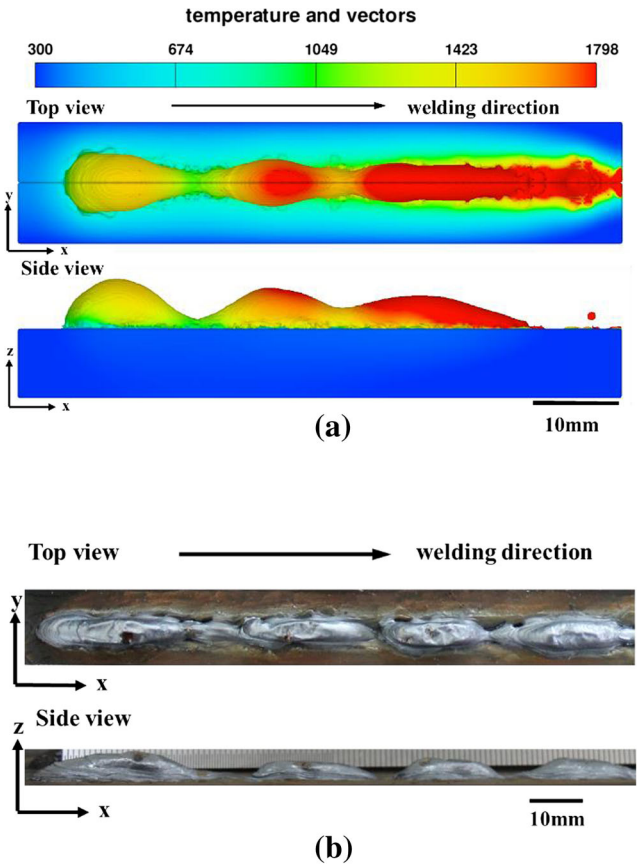

Fig. 3 **a** Simulated bead. **b** Experimental bead

general shape as the experimental one, both of which consist of humps and valleys.

Table 2 shows the bead parameters obtained by simulations and experiments. Within the deviation limits, the simulated bead parameters are close to the experimental ones. The discrepancy in shapes of humped bead is due to large numbers of assumptions and the errors in material properties and boundary conditions. Based on the results above, more studies are conducted to analyze the hump formation mechanism in this paper.

Figure 4 demonstrates the dynamic development of the simulated weld pool shape and flow field on longitudinal cross section of the workpiece as well as the images obtained by high-speed camera in four moments ($t = 0.7$, 0.85, 1.1, 1.25 s). The weld pool is represented by red areas in simulations and bright areas in high-speed camera images.

As is shown in Fig. 4, the weld pool t changes greatly with impact of arc pressure and droplet impinging force at 0.7 s. A large gouged region is formed below the arc, which has a thin layer of molten metal in it. When the molten metal flow, which has great backward momentum, goes through the middle part of the weld pool, little metal is left because of the high welding speed. Then large amount of molten metal is brought to the pool tail, where the fluid flow turns slow and calm, forming a swelling region. Thus, a thin and narrow liquid channel emerges between the gouged region and the pool tail.

At 0.85 s, the liquid channel is elongated while the pool tail is still swelling. At 1.1 s, the liquid channel turns thinner and starts pinching. At 1.25 s, the liquid channel solidifies while the other parts of the weld pool are still above melting point. The solidification of liquid channel divides the weld pool into two parts, restricting the reflux of molten metal from the pool tail, which will become the first hump after solidified. The solidified liquid channel is called the first valley as well. Then the front part of the weld pool will repeat the similar process of hump formation as before.

The dynamic actions of liquid channel are the significant factor of hump formation. It has four stages: formation, elongation, pinching, and solidification.

As is shown in Fig. 5, the liquid channel begins forming as molten metal accumulates in this region at 0.7 s. In this paper, cross-sectional view at $x = 20$ mm is taken into study. It is

Table 2 Bead parameters by simulation and experiment

Reference (mm)	Predicted	Measured
Hump width	6.70	7.62
Valley width	5.40	6.97
Penetration	2.21	2.46
Hump height	5.69	4.94
Valley eight	1.33	1.56

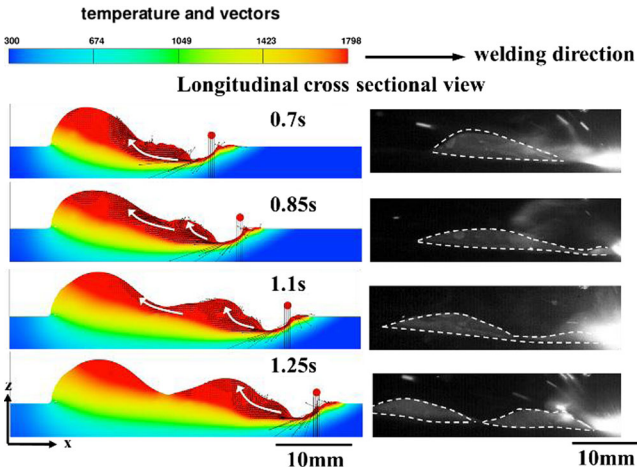

Fig. 4 The longitudinal cross-section view of simulated weld pool shape and the flow field and the images obtained by high-speed camera

found that the molten metal flows upward and outward with the effect of Marangoni force. During 0.7 to 0.85 s, the liquid channel is constantly elongated and the cross section of the weld pool gradually swells because of the high welding speed. At this time, the fluid flow direction does not change much but the outward component becomes smaller than the initial stage. According to the capillary instability theory [16], when the

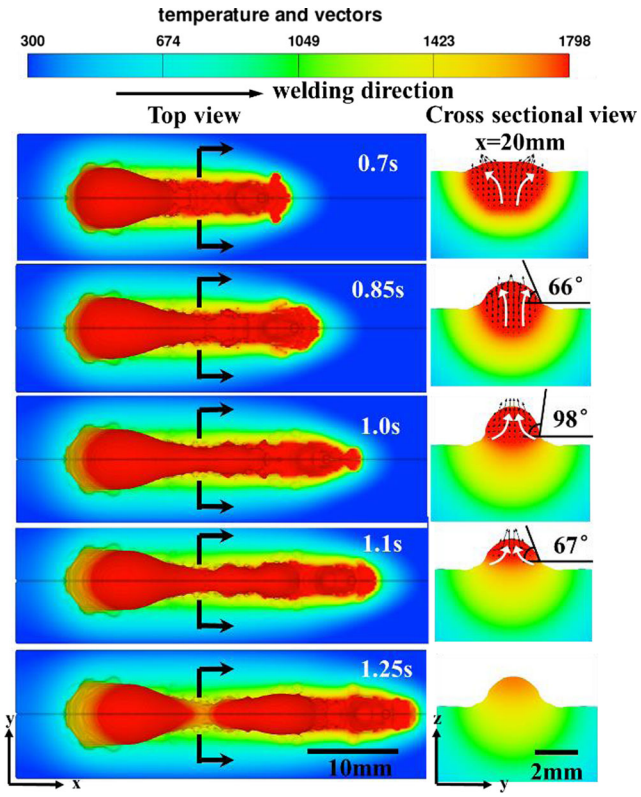

Fig. 5 0.7–1.25 s top view of the simulated weld pool and the cross-sectional view at $x = 20$ mm

internal contact angle is less than π/2, the weld pool is considered in a stable state. Otherwise, the weld pool is more likely to collapse due to the stronger oscillation. Therefore, the weld pool is stable at 0.85 s as the contact angle is 66°. As time goes on, the contact angle increases from 66° to 98° during 0.85 to 1.0 s, because of which the weld pool turns into unstable state from the initial stable state. The normal vector of surface tension, which plays significant role in maintaining the weld pool's stability, is proportion to the cross section curvature and it approximately points to the curvature center of the cross section. At 1.0 s, the normal surface tension is strong due to the great cross section curvature, leading to the pinching of the cross section of the weld pool. With the impact of the normal surface tension, the molten metal flows to the center of the cross section from 1.0 to 1.1 s. The contact angle of the cross section gradually decreases until it is less π/2 and the weld pool returns stable again. Comparing to the cross section of weld pool at 0.85 s, it is obviously narrower and has a smaller curvature. Thus, the normal surface tension becomes small as well. Because of the force balance in the cross section of weld pool, rarely strong oscillations occur afterward.

At 1.25 s, the liquid channel starts solidification at $x = 20$ mm, dividing the weld pool into two parts. The reasons responsible for the liquid channel's early solidification can be listed below:

1. There is less molten per unit length in liquid channel region due to the pinching of the weld pool's cross section, which means the liquid channel contains less heat enthalpy per unit length.
2. The liquid channel is elongated by the high welding speed, which is kept far away from the heat input region and unable to directly obtain the heat of the arc. Thus, it turns to be the relatively low temperature region and has the highest cooling rate, which leads to its solidification in advance.

The formation, elongation, pinching, and early solidification are the four significant stages in hump formation, which can be observed both by simulations and high-speed camera. Based on the analyses above, the strong backward molten metal flow and the impact of the normal surface tension are concluded as the major factor of the dynamic actions of the liquid channel. Thus, reducing the backward momentum of molten metal flow is considered as one of the effective methods to suppress hump formation.

4.2 Studies of hump suppression in triple-wire GMAW

The simulation results of bead-on-plate shape in high-speed triple-wire GMAW are shown in Fig. 6a and the experimental ones are shown in Fig. 6b. Table 3 shows the bead parameters

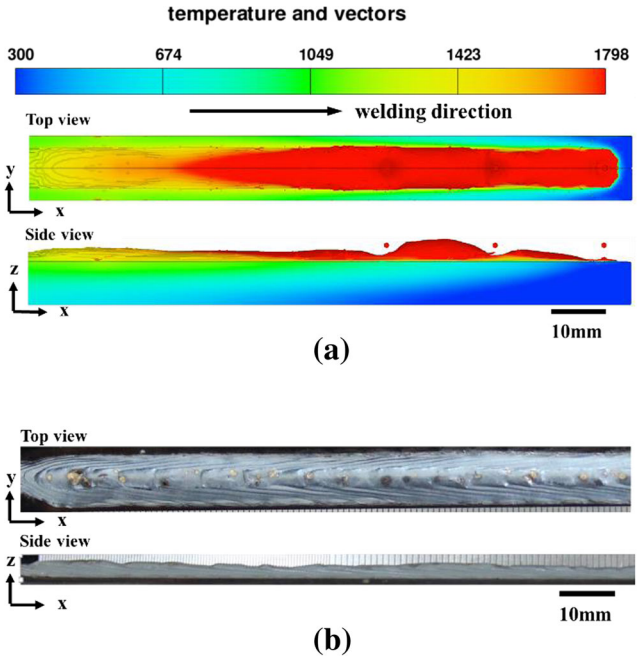

Fig. 6 **a** Simulated bead. **b** Experimental bead

obtained by simulations and experiments. It indicates that the simulated bead is similar to the experimental one. Within the deviation limits, the simulated bead parameters are in good agreement with the experimental ones. Besides the reasons mentioned in Section 4.1, ignoring the interference between arcs in multi-wire welding is another factor in the discrepancy, which is to be studied in the future work.

Different from the hump bead formed in single-wire GMAW, a sound bead is formed without humps and valleys in triple-wire GMAW. The triple-wire GMAW has a higher welding speed (2.7 m/min) under the same line energy with the single-wire GMAW, which proves the possibility of hump suppression by triple-wire GMAW.

As is shown in Figs. 7 and 8, the weld pool of high-speed triple-wire GMAW is quite different from that of single-wire GMAW, which has three sub-weld pools: leading weld pool, middle weld pool, and trailing weld pool. Although the three sub-weld pools are separated by the middle arc and the trailing arc, they are all connected with each other. Neither elongated and narrow liquid channel nor solidification in advance of liquid channel is observed during the triple-wire GMAW

Table 3 Bead parameters by simulation and experiment

Reference (mm)	Predicted	Measured
Width	8.15	9.13
Penetration	1.80	1.72
Height	2.38	2.46

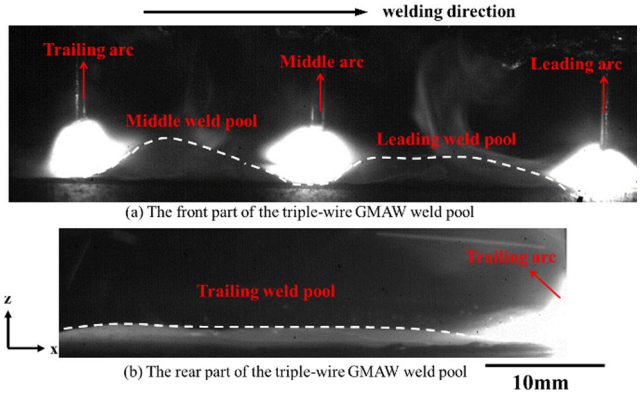

Fig. 7 Images of the triple-wire GMAW weld pool obtained by high-speed camera

process as the weld width keeps consistent along the welding direction. The contact angles of the cross sections captured from the three sub-weld pools are all less than $\pi/2$, which means the three sub-weld pools are all in stable state and less likely to collapse or pinch. According to the analysis above, it can be proved that the weld pool keeps a stable state during high-speed triple-wire GMAW.

Nguyen et al. [6, 7] and Hu et al.'s [17] investigations found that any method which can reduce the momentum of the backward molten metal flow can make a difference in suppressing humps. The "pull-push" flow observed in the weld pool of high-speed triple-wire GMAW is considered to play a significant role in dramatically slowing down backward trend of the molten metal flow.

In the front part of the leading weld pool, the molten metal flows backward with the impact of the leading wire's arc pressure and droplet impinging force while in the tail of the leading weld pool, the molten metal flows forward with the impact of the middle wire's arc pressure and droplet impinging force, restricting the backward flow from the front part of the weld

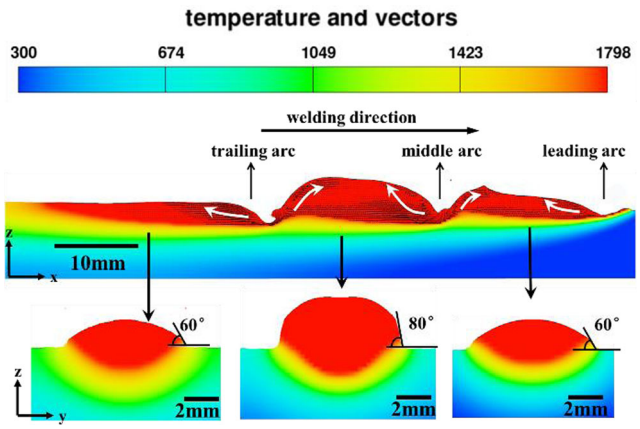

Fig. 8 The longitudinal cross-section view of simulated weld pool shape and the flow field and the cross-sectional views of three sub-weld pools ($t = 1.4$ s)

pool. In this way, a pull-push flow is formed caused by these two flows of different directions and the molten metal accumulates in the pool tail, resulting the swelling of the pool tail and increasing the residence time of molten metal in the weld pool.

There is similar pull-push flow in the middle weld pool. Due to the preheating effect and additional molten metal derived from the leading weld pool, the middle pool is higher than the leading one and holds the most molten metal.

Different from the first two weld pools, there is only backward flow in the trailing weld pool. However, the flow is quite steady and the height of the trailing weld pool remains unchanged. It is because that the pull-push flow in leading and middle weld pools has slowed down the backward trend of the molten metal, increased its residence time, and reduced its solidification rate. The hump defect cannot be formed for no conditions of liquid channel's appearance. On the other hand, arc pressures and droplet impinging forces are dispersed along the weld pool, for which the weld pool has a uniform deformation and the welding process maintains steady.

5 Conclusion

In this paper, a three-dimensional numerical model of transient weld pool was established using the finite element software FLOW-3D. Analyzing the simulated temperature field and fluid flow field in the high-speed single-wire GMAW and the triple-wire GMAW, the following two conclusions could be drawn:

1. The simulated bead was in good agreement with the experimental one within deviation limits in high-speed (1.5 m/min) single-wire GMAW. The results of simulations and high-speed camera images illustrated that the formation, elongation, pinching, and early solidification of the liquid channel were observed as the four significant stages in hump formation. The strong backward molten metal flow and the impact of the normal surface tension were concluded as the major factor of the dynamic actions of the liquid channel.
2. The simulated bead was in good agreement with the experimental one within deviation limits in high-speed (2.7 m/min) triple-wire GMAW, which was of the same line energy with the single-wire GMAW. The results show that the pull-push flow in the weld pool could dramatically slow down the backward trend of the molten metal, increased its residence time, and reduced its solidification rate. Thus, the hump defect was suppressed for none conditions of liquid channel's appearance. It was proved that the pull-push flow could improve the stability of welding process.

Acknowledgments This work gained financial supports from the National Natural Science Foundation of China. The award number is 51275229.

References

1. Olsson R, Stemvers M, Staers I (1995) High-speed welding gives a competitive edge. Weld Rev Int 14(8):128–131
2. Lucas B (1997) FCAW, multiwire and gas selection: techniques to enhance MIG productivity. Weld Met Fabr 65(5):10–12
3. Ma X, Lin H, Hua X, Wu Y (2013) Full factorial design on triple-electrode high speed CO2 fillet welding on double sides. Trans Chin Weld Inst 5:025
4. Wu, D., Hua, X., Ye, D., Ma, X., & Li, F. (2016). Understanding of the weld pool convection in twin-wire GMAW process. The International Journal of Advanced Manufacturing Technology, 1-9. Doi: 10.1007/s00170-016-8775-1
5. Bradster BJ (1968) Effect of surface tension and metal flow on weld bead formation. Weld J 47(7):S314
6. Nguyen TC, Weckman DC, Johnson DA, Kerr HW (2005) The humping phenomenon during high speed gas metal arc welding. Sci Technol Weld Join 10(4):447–459
7. Nguyen TC, Weckman DC, Johnson DA (2007) Predicting onset of high speed gas metal arc weld bead defects using dimensional analysis techniques. Sci Technol Weld Join 12(7):634–648
8. Cho MH, Farson DF (2007) Understanding bead hump formation in gas metal arc welding using a numerical simulation. Metall Mater Trans B 38(2):305–319
9. Chen MJ, Wu CS (2010) Numerical analysis of forming mechanism of hump bead in high speed GMAW. Weld World 54(9-10): R286–R291
10. Chuansong CJW (2009) Numerical simulation of forming process of humping bead in high speed GMAW. Acta Metall Sin 45(9): 1070–1076
11. Yokota MY, Shimizu MH, Nagaoka MS, Ito MK, Arita MH (2012) Development and application of the 3-electrode MAG high-speed horizontal fillet welding process. Weld World 56(1-2):43–47
12. Lin H, Hua X, Ma X, Wang F, Wu Y, Oniki Y, Shi J (2008) Effect of welding speed and current on weld geometry in triple electrode high-speed CO2-shielded welding process. Hot Work Technol 23: 029
13. Song Wu C, Tsao KC (1990) Modelling the three-dimensional fluid flow and heat transfer in a moving weld pool. Eng Comput 7(3): 241–248
14. Goldak J, Chakravarti A, Bibby M (1984) A new finite element model for welding heat sources. Metall Trans B 15(2):299–305
15. Sahoo P, DebRoy T, McNallan MJ (1988) Surface tension of binary metal-surface active solute systems under conditions relevant to welding metallurgy. Metall Trans B 19(3):483–491
16. Cho DW, Na SJ, Cho MH, Lee JS (2013) A study on V-groove GMAW for various welding positions. J Mater Process Technol 213(9):1640–1652
17. Hu ZK, Wu CS (2008) Experimental investigation of forming process of humping bead in high speed MAG arc welding. Acta Metall Sin 44(12):1445–1449